

THEORETICAL ANALYSIS OF ELECTROSTATIC ENERGY HARVESTER CONFIGURED AS BENNET'S DOUBLER BASED ON Q-V CYCLES

Binh Duc Truong, Cuong Phu Le and Einar Halvorsen

Keywords: *Q-V cycle, Bennet's doubler, saturation voltage, electrostatic energy harvester.*

Abstract – This paper presents theoretical analysis of a MEMS electrostatic energy harvester configured as the Bennet's doubler. Steady-state operation of the doubler circuit can be approximated by a right-angled trapezoid Q-V cycle. A similarity between voltage doubler and resistive-based charge-pump circuit is highlighted. By taking electromechanical coupling into account, the analytical solution of the saturation voltage is the first time derived, providing a greater comprehension of the system performance and multi-parameter effects. The theoretical approach is verified by results of circuit simulation for two cases of mathematically idealized diode and of Schottky diode. Development of the doubler/multiplier circuits that can further increase the saturation voltage is investigated.

1. INTRODUCTION

Wireless sensor nodes (WSNs) are emerging as one of the most commonly used monitoring and sensing systems [1, 2]. Currently, most WSNs are powered by batteries. Energy harvesting from vibration becomes a potential alternative to obtain electrical energy for WSNs, especially in some circumstances where batteries may not be feasible. For the vibration energy harvesters, there are three common transduction mechanisms which includes piezoelectric, electromagnetic and electrostatic [3–5]. In this paper, we focus on the electrostatic energy harvesting system.

One of the problems associated with the electrostatic energy harvesters is the implementation of power management circuits. As an example, a conversion circuit consisted of a voltage source, a variable capacitor and two switches was presented in [6, 7]. Although energy transduction through this circuit is possible, the regime where the output voltage saturated was not discussed. Several solutions based on energy-renewal technique for extracting electrical energy were presented. For instance, Yen *et al.* proposed a configuration of single variable-capacitance harvester, combining an asynchronous charge-pump with an inductive fly-back circuit to recharge the scavenging capacitor [8]. Mitcheson *et al.* developed a buck-boost topology with bi-directional switches for rectifying and increasing the AC voltage obtained from a transducer [9]. These circuit topologies face the trade-off between power consumption of control unit and harvester efficiency.

The Bennet's doubler was early introduced in 1787 by the Reverend Bennet and Kaye [10]. The device is used for the continuous doubling of an initial small charge through a sequence of operations with three plates. Based on this approach, de Queiroz proposed a promising variation of such a voltage doubler for macro-scale vibration energy harvesters composed by variable capacitors and diodes [11–13]. In order to adapt the concept to micro-scale electrostatic generators, several researches have been developed and investigated [14–17], including attempts to increase the charging current for a reservoir capacitor or to optimize the harvested power. In a recent work by Galayko [18], operation of the doubler configuration with a single variable capacitor was thoroughly analyzed in the electrical domain. The shape of Q-V diagram obtained from simulation is very close to be

rectangular. However, operation of a transducer configuration with two time-varying capacitors and the dependence of the saturated voltage on dynamic characteristics of the mechanical domain has not explored yet.

Since the saturation phenomenon was observed in experiments [16], the effect of the electromechanical coupling on it is of interest to study. This paper further presents a theoretical analysis of the Bennet's doubler based on the Q-V cycle. A complete model of an anti-phase overlap-varying transducers electrically configured as a voltage doubler is investigated. Numerical results for both ideal- and non-ideal diodes are obtained by means of a SPICE simulator, which are used to support the analytical solutions. For further increase of the saturated voltage across the storage capacitor, alternative topologies are introduced and analyzed.

2. STEADY STATE OPERATION WITH MATHEMATICALLY IDEALIZED DIODES

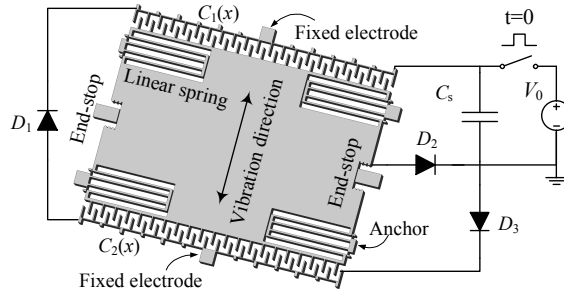


FIGURE 1. Overlap-varying energy harvesters employing the Bennet's doubler circuit.

2.1. Theoretical analysis. The overlap-varying energy harvesters can be utilized in a charge-doubling circuit-configuration as shown in Figure 1. The proof mass is suspended by four folded-beam linear springs. The maximum displacement X_{\max} is defined by the mechanical end-stops. Two anti-phase variable capacitors $C_{1/2}(x) = C_0(1 \mp \frac{x}{x_0})$ are connected to three diodes D_1, D_2, D_3 and the storage capacitor C_s . Here C_0, x_0 and x are the nominal capacitance, the nominal overlap and the proof mass displacement respectively. Operation of the doubler circuit does not require any control unit or switches but an initial bias voltage V_0 .

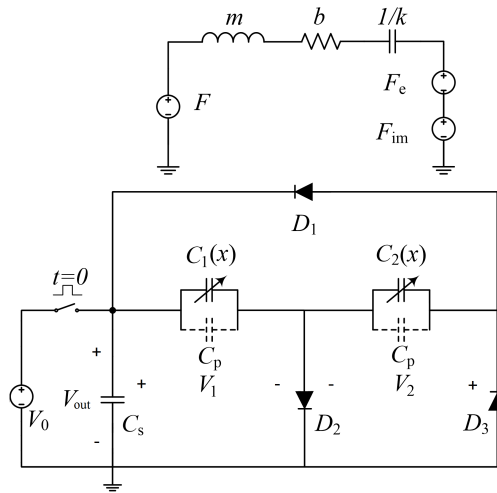


FIGURE 2. Equivalent circuit for mechanical domain and Bennet's doubler configuration.

TABLE 1. Model parameters

Parameters	Value
Proof mass, m	1.022 mg
Spring stiffness, k	3.595 N/m
Thin-film air damping, b	3.478e-5 Ns/m
Nominal overlap, x_0	80 μm
Nominal capacitance, C_0	15 pF
Parasitic capacitance, C_p	7.5 pF
Storage capacitance, C_s	10 nF
Contact stiffness, k_{im}	3.361 MN/m
Impact damping, b_{im}	0.435 Ns/m
Maximum displacement, X_{max}	80 μm

Figure 2 shows a complete lumped-model of the doubler configuration including equivalent circuit for the mechanical subsystem, where m - proof mass, b - mechanical damping, k - total spring stiffness, F - an external force, F_e - the electrostatic force and C_p - the parasitic capacitance of each transducer. The contact force F_{im} is simply modeled as a spring-damper system $F_{\text{im}} = k_{\text{im}}\delta + b_{\text{im}}\dot{\delta}$ for $|x| \geq X_{\text{max}}$ [19], where $\delta = |x| - X_{\text{max}}$ is relative displacement between the proof mass and the end-stops, k_{im} is the impact stiffness and b_{im} is the impact damping. For a sufficient voltage V_0 and

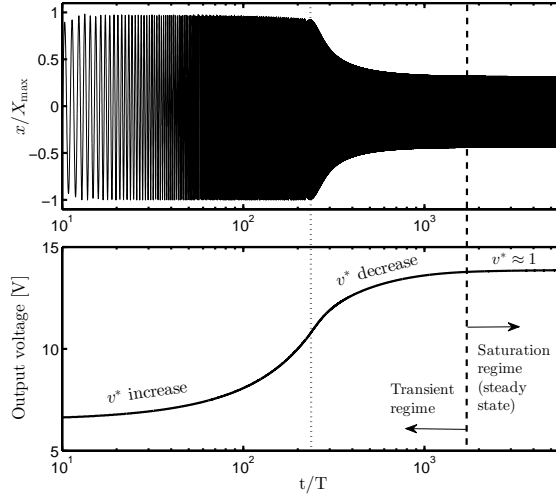


FIGURE 3. Evolution of the proof mass displacement and the output voltage across the storage capacitor with the input acceleration amplitude $A = 2.0$ g, the drive frequency $f = f_0$ and the initial bias voltage $V_0 = 7$ V.

an adequate input acceleration amplitude A , the voltage accumulated on the storage capacitor C_s initially increases. The vibration frequency is chosen $f = f_0 = \frac{1}{2\pi} \sqrt{\frac{k}{m}}$. Figure 3 shows that after certain cycles of transient regime, the steady state is achieved. The electrical energy is no longer harvested and the output voltage V_{out} is then maintained constant at V_s (i.e., saturation voltage).

The proof mass displacement amplitude X_0 changes in complicated manner: X_0 first reaches the maximum value $X_0 \approx X_{\text{max}}$ (i.e., which is limited by the mechanical end-stops), then decreases and kept fixed at $X_0 \approx X_s$ in saturation regime. For convenience, we define the rate of voltage

evolution v^* as a ratio of the maximum output voltage in two subsequent period

$$(2.1) \quad v^* = \frac{\max(V_{\text{out}}|_{T_{i+1}})}{\max(V_{\text{out}}|_{T_i})}.$$

As shown in Figure 3, v^* is modified over cycles under the variation of X_0 as follows. v^* is small at the beginning and gradually increases, meanwhile $X_0 \approx X_{\text{max}}$. After reaching the maximum, v^* decreases with reduction of X_0 and finally becomes one at steady state. Ultimately higher voltages through the conversion phase induce more effective electrical damping represented by electrostatic force in the transducers, causing a decrease of the proof mass displacement. As a consequence, the transducer capacitance ratio is reduced to $\eta = (C_{\text{max}} + C_p)/(C_{\text{min}} + C_p) \approx 1.72$, which is no more satisfied the condition of the doubler circuit operation $\eta_{\text{cr}} = 2$. Therefore, V_{out} is saturated at a certain value. Detail of dynamic analyses and the model parameters (i.e., listed in Table 1) are referred to [20]. In this paper, the effect of the electrostatic force on V_s is the major objective of investigation.

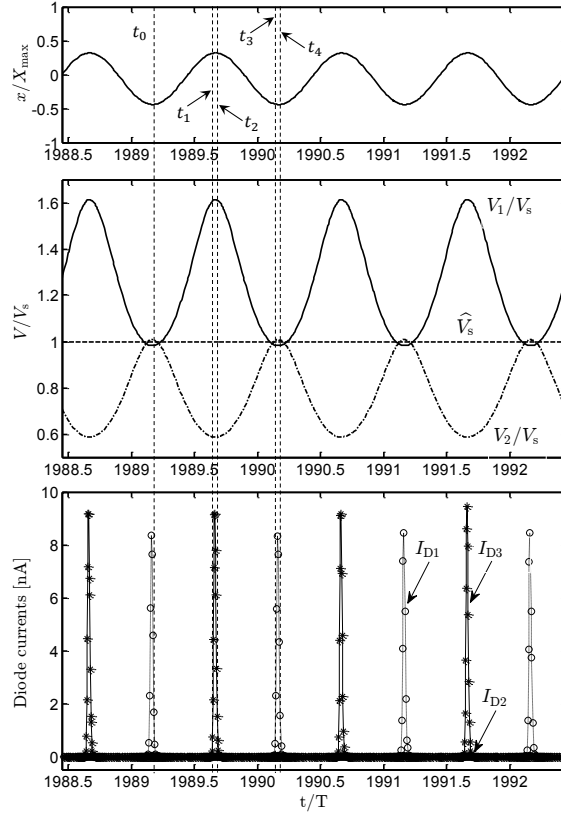


FIGURE 4. Waveforms of displacement, voltages on variable capacitors and currents through three diodes at steady state with $A = 2.0$ g and $f = f_0$.

Figure 4 shows waveforms of the proof mass displacement, the voltages V_1 , V_2 across C_1 , C_2 and the currents I_{D1} , I_{D2} , I_{D3} through three mathematically idealized diodes respectively. Operation of the doubler circuit at steady state can be divided into a sequence of four stages from t_0 to t_4 . Based on the dynamic simulations, we observe that the relation of Q_1 and V_1 at steady state can be approximated by a right-angled trapezoid Q-V cycle diagram and the time interval between $\Delta t_{21} = t_2 - t_1$ and $\Delta t_{43} = t_4 - t_3$ are very small, as depicted in Figure 5.

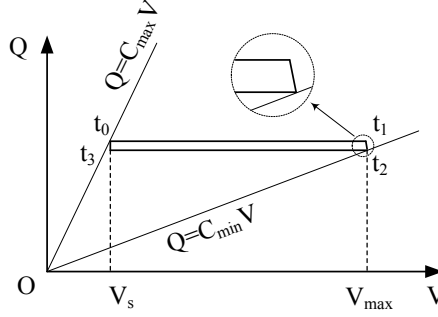


FIGURE 5. Approximated Q-V diagram of variable capacitor $C_1(x)$ at steady state with mathematically ideal diodes.

Stage I:

At $t = t_0$, $x(t_0) = -X_s$ and $V_1(t_0) \approx V_2(t_0) \approx V_s$, where X_s is the maximum displacement at steady state. From t_0 to t_1 , all three diodes D_1 , D_2 and D_3 are blocking as the condition $V_{C_2} < V_0 < V_{C_1} < V_{C_2} + V_0$ is satisfied. The charges on the two transducers are

$$(2.2) \quad q_1(t_0) = V_s \left[C_p + C_0 \left(1 + \frac{X_s}{x_0} \right) \right],$$

$$(2.3) \quad q_2(t_0) = V_s \left[C_p + C_0 \left(1 - \frac{X_s}{x_0} \right) \right].$$

In the first stage, q_1 and q_2 are constants, V_1 and V_2 are given

$$(2.4) \quad V_1 \Big|_{t \in [t_0, t_1]} = \frac{q_1}{C_1} = \frac{V_s \left[C_p + C_0 \left(1 + \frac{X_s}{x_0} \right) \right]}{C_p + C_0 \left(1 - \frac{x}{x_0} \right)},$$

$$(2.5) \quad V_2 \Big|_{t \in [t_0, t_1]} = \frac{q_2}{C_2} = \frac{V_s \left[C_p + C_0 \left(1 - \frac{X_s}{x_0} \right) \right]}{C_p + C_0 \left(1 + \frac{x}{x_0} \right)}.$$

Stage II:

At $t = t_1$, $V_1(t_1) \approx V_2(t_1) + V_s$ and diode D_3 starts to conduct. Since the time interval between t_1 and t_2 is very small (i.e., see Figure 5), the proof mass displacement at t_1 can be approximated as $x(t_1) \approx x(t_2) = X_s$, then

$$(2.6) \quad \frac{1 + \frac{C_0}{C_p} \left(1 + \frac{X_s}{x_0} \right)}{1 + \frac{C_0}{C_p} \left(1 - \frac{X_s}{x_0} \right)} = 1 + \frac{1 + \frac{C_0}{C_p} \left(1 - \frac{X_s}{x_0} \right)}{1 + \frac{C_0}{C_p} \left(1 + \frac{X_s}{x_0} \right)}.$$

The solution is given as

$$(2.7) \quad X_s = 3 \left(\frac{\sqrt{5}}{2} - 1 \right) x_0.$$

The peak values of voltages across C_1 and C_2 are

$$(2.8) \quad V_I = V_1(t_1) = V_1(t_2) = V_s \frac{\sqrt{5} + 1}{2},$$

$$(2.9) \quad V_{II} = V_2(t_1) = V_2(t_2) = V_s \frac{\sqrt{5} - 1}{2}.$$

In this stage, charges ΔQ_s and ΔQ are pumped from C_1 into C_s and C_2 respectively. At steady state, V_s is considered unchanged, thus ΔQ_s is neglected.

Stage III:

From t_2 to t_3 , all diodes are blocked, q_1 and q_2 are constants

$$(2.10) \quad q_1 \Big|_{t \in [t_2, t_3]} = q_1(t_2) = V_s \left[C_p + C_0 \left(1 + \frac{X_s}{x_0} \right) \right] - \Delta Q,$$

$$(2.11) \quad q_2 \Big|_{t \in [t_2, t_3]} = q_2(t_2) = V_s \left[C_p + C_0 \left(1 - \frac{X_s}{x_0} \right) \right] + \Delta Q.$$

At t_3 , $x(t_3) = x_3$, $V_1(t_3) = V_s$ (2.12) and D_2 starts to conduct transferring amount of charge ΔQ^* from C_s into C_1 . Similarly, since V_s is treated as constant, ΔQ^* is thus negligible. The relation (2.12) now can be written as

$$(2.13) \quad V_1(t_3) = \frac{q_1(t_3)}{C_1(t_3)} = \frac{V_s \left[C_p + C_0 \left(1 + \frac{X_s}{x_0} \right) \right] - \Delta Q}{C_p + C_0 \left(1 - \frac{x_3}{x_0} \right)} = V_s.$$

Due to the small interval time between t_3 and t_4 , $x_3 \approx x(t_4) = -X_s$, resulting in $\Delta Q \approx 0$. In other words, the charge transferred from C_1 into C_2 is insignificant.

Considering the voltage across the capacitor C_2 at t_3

$$(2.14) \quad V_2(t_3) = \frac{q_2(t_3)}{C_2(t_3)} = \frac{V_s \left[C_p + C_0 \left(1 - \frac{X_s}{x_0} \right) \right] + \Delta Q}{C_p + C_0 \left(1 + \frac{x_3}{x_0} \right)} \approx V_s.$$

Therefore, D_1 also starts to conduct at t_3 since the condition $V_2 \approx V_s$ holds.

Stage IV:

From t_3 to t_4 , D_1 is conducting and ΔQ is transferred from C_2 into C_1 . The charge q_4 is

$$(2.15) \quad q_1(t_4) = q_1(t_3) + \Delta Q = V_s \left[C_p + C_0 \left(1 + \frac{X_s}{x_0} \right) \right].$$

The condition $q_1(t_4) = q_1(t_0)$ (2.16) is fulfilled, showing that the state of the doubler circuit at t_4 is exactly the same as when $t = t_0$, and a new cycle starts. This also proves that the right-angled trapezoid Q-V cycle diagram is capable of describing the operation of the doubler circuit.

2.2. Similarity of Bennet's doubler and charge-pump circuit. Among different circuit topologies for the interface electronics of MEMS capacitive energy harvesters [21, 22], the charge pump circuit early presented by Roundy *et al.* [23] is one of the most promising topologies. Another variation with inductive fly-back circuitry was developed by Yen *et al.* [8]. The simplest way to implement fly-back is to use a load resistance, originally reported in [24]. Such a fly-back configuration was thoroughly analyzed in [25].

Comparing the results shown in the literature with the one obtained in this paper, it is worth to note that the Q-V cycle for the charge pump circuit with resistive fly-back is very similar to that of Bennet's doubler circuit. Both topologies can be approximated by trapezoidal conversion cycle. At the steady state of the idealized charge pump and the voltage doubler, the Q-V cycle is degenerated to a line (i.e., see Figure 5).

3. APPROXIMATION OF THE SATURATION VOLTAGE WITH MATHEMATICALLY IDEAL DIODE

The electrostatic force F_e plays an important role in saturation of the output voltage and is thoroughly analyzed in this Section. F_e is modeled as

$$(3.1) \quad F_e = -\frac{\partial W_e}{\partial x} = -\frac{1}{2} \frac{\partial C_1(x)}{\partial x} V_1^2 - \frac{1}{2} \frac{\partial C_2(x)}{\partial x} V_2^2 = \frac{1}{2} \frac{C_0}{x_0} (V_1^2 - V_2^2)$$

where W_e is the electrostatic energy of the transducers. V_1 and V_2 can be simplified as anti-phase sinusoidal signals for the sake of analysis although it is more complicated than that in reality. Based

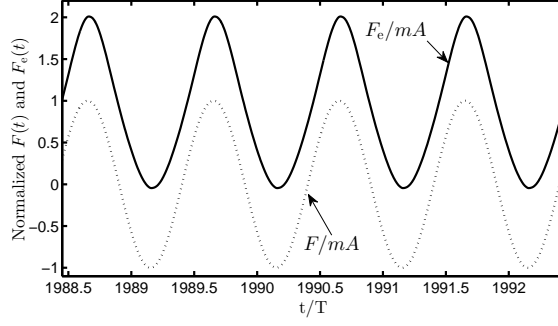


FIGURE 6. Normalized waveforms of the input acceleration in comparison with the electrostatic force obtained from simulation.

on the dynamic simulations, we observe that the phase difference between *the input acceleration* and *the voltage across C_1* is negligibly small and is ignored. The waveforms of V_1 and V_2 are then presented as

$$(3.2) \quad V_1 = \frac{V_I + V_s}{2} + \frac{V_I - V_s}{2} \sin(\omega t) = V_s \frac{3 + \sqrt{5}}{4} + V_s \frac{-1 + \sqrt{5}}{4} \sin(\omega t),$$

$$(3.3) \quad V_2 = \frac{V_{II} + V_s}{2} - \frac{V_s - V_{II}}{2} \sin(\omega t) = V_s \frac{1 + \sqrt{5}}{4} - V_s \frac{3 - \sqrt{5}}{4} \sin(\omega t)$$

yielding

$$(3.4) \quad V_1^2 - V_2^2 = \frac{2 + \sqrt{5}}{4} V_s^2 (1 + \sin(\omega t)) \left(1 + \frac{(\sqrt{5} - 2)^2}{2} \sin(\omega t) \right).$$

The coefficient $\frac{(\sqrt{5}-2)^2}{2} \approx 0.028 \ll 1$ is negligible, the electrostatic force is then

$$(3.5) \quad F_e = \frac{2 + \sqrt{5}}{8} \frac{C_0}{x_0} V_s^2 (1 + \sin(\omega t)) = F_0 (1 + \sin(\omega t)).$$

where $F_0 = \frac{2 + \sqrt{5}}{8} \frac{C_0}{x_0} V_s^2$. The harmonic term of F_e is in phase with the input acceleration.

Figure 6 shows the comparison between the input acceleration and the electrostatic force, at the same time duration as Figure 4. These simulation results along with expression of F_e in (3.5) confirm that our assumption is reasonable.

The differential equation of the spring-mass-damping system, which is set in continuous oscillation by a sinusoidal force acting on the mass, is

$$(3.6) \quad m\ddot{x} + b\dot{x} + kx = mA \sin(\omega t) - F_e.$$

The steady-state solution of (3.6) is $x = -\bar{x} + x_h$, where $\bar{x} = \frac{F_0}{k}$ is the offset displacement and the harmonic term is [26]

$$(3.7) \quad x_h = X_0 \sin(\omega t + \varphi).$$

where $X_0 = \frac{(mA - F_0)/m}{\sqrt{(\omega^2 - \omega_0^2)^2 + (\frac{b}{m})^2 \omega^2}}$. Since $\omega = \omega_0 = \sqrt{\frac{k}{m}}$ and the proof mass displacement barely

reaches its constraint, the peak value of x_h is $X_0 = X_s = \frac{mA - F_0}{b\omega_0}$. The ratio $\frac{\bar{x}}{X_0}$ obtained from simulations is less than 2.1% for all $A \in [1, 2]$ g, therefore \bar{x} is assumed negligible. By considering

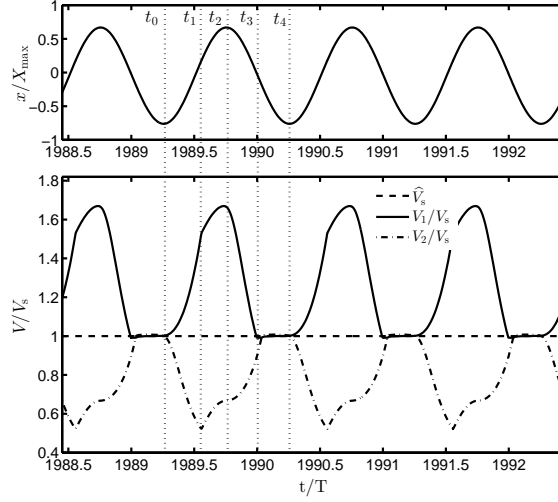


FIGURE 7. Normalized displacement and voltage waveforms on variable capacitors $C_1(x)$ and $C_2(x)$ at saturation with the input external acceleration $A = 2.0$ g.

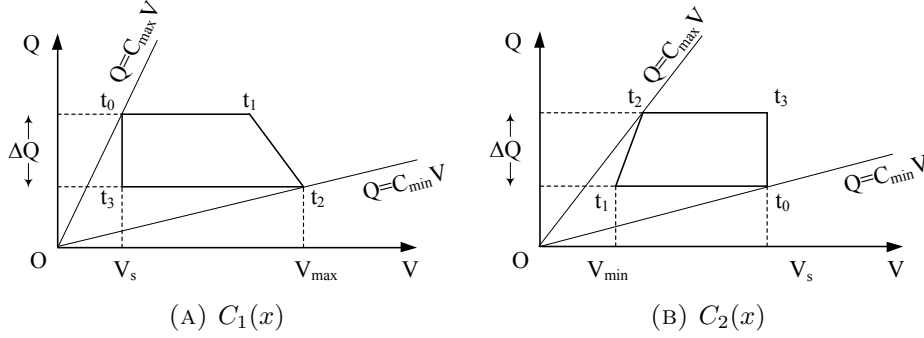


FIGURE 8. Generally approximated Q-V diagram of Bennet's doubler at saturation for both transducers.

amplitudes of the harmonic term and ignoring phase differences, the saturation voltage is

$$(3.8) \quad V_s = \sqrt{\frac{8}{2 + \sqrt{5}} \frac{mA - \frac{3}{2}(\sqrt{5} - 2)x_0 b \omega_0}{\frac{C_0}{x_0}}}$$

Although performance of the harvesting system using mathematically ideal diode is analyzed, the power loss due to diode imperfections such as leakage current and junction capacitance is still an open room for investigation. This issue will be explored in the next section.

4. OPERATION OF THE BENNET'S DOUBLER WITH SCHOTTKY DIODE

4.1. Approximated Q-V Cycle at steady state. In the same manner of the Dragunov's work [14, 27], the Schottky diode 1N6263 is used to assess effect of diode losses on the harvesting system performance, where the magnitude of reverse current is comparable with the charging current through the storage capacitor, and the zero bias junction capacitance is in the range of transducer nominal capacitance.

Figure 7 shows waveforms of the proof mass displacement and the voltages V_1 and V_2 across C_1 and C_2 respectively. Similarly, operation of the doubler circuit at steady state can be divided into

a sequence of four stages, which is more clearly than considerations of mathematically idealized diode (i.e., the time interval between stages is significant). In general, the relation of Q_1 (Q_2) and V_1 (V_2) at steady state can be approximated by a right-angled trapezoid Q-V cycle diagram in Figure 8. Charges transferred from or into C_s are neglected since the output voltage is unchanged at steady state. Differently from previous section, the proof mass displacements at t_1 and t_3 are still unknown.

Stage I:

The same as previous analysis, the charges on the two generators and variations of V_1 and V_2 from t_0 to t_1 are presented by equations (2.2), (2.3), (2.4) and (2.5).

Stage II:

At $t = t_1$, $x(t_1) = x_1$, $V_1(t_1) = V_2(t_1) + V_s$ and diode D_3 starts to conduct, this yields

$$(4.1) \quad \frac{1 + \frac{C_0}{C_p} \left(1 + \frac{X_s}{x_0}\right)}{1 + \frac{C_0}{C_p} \left(1 - \frac{x_1}{x_0}\right)} = 1 + \frac{1 + \frac{C_0}{C_p} \left(1 - \frac{X_s}{x_0}\right)}{1 + \frac{C_0}{C_p} \left(1 + \frac{x_1}{x_0}\right)}.$$

From t_1 to t_2 , charge ΔQ is pumped from C_1 into C_2 .

Stage III:

From t_2 to t_3 , all diodes are blocked, q_1 and q_2 are constants that are described by (2.10) and (2.11). At $t = t_3$, D_2 starts to conduct due to $V_1(t_3) = V_s$ (4.2). This condition is expressed by (2.13), which results in

$$(4.3) \quad \Delta Q = V_s C_0 \left(\frac{X_s + x_3}{x_0} \right).$$

The voltage across C_2 at t_3 is

$$(4.4) \quad V_2(t_3) = \frac{q_2(t_3)}{C_2(t_3)} = \frac{V_s \left[C_p + C_0 \left(1 - \frac{X_s}{x_0}\right) \right] + \Delta Q}{C_p + C_0 \left(1 + \frac{x_3}{x_0}\right)} = \frac{V_s \left[C_p + C_0 \left(1 - \frac{X_s}{x_0}\right) \right] + V_s C_0 \left(\frac{X_s + x_3}{x_0} \right)}{C_p + C_0 \left(1 + \frac{x_3}{x_0}\right)} = V_s.$$

As the condition $V_2 = V_s$ is fulfilled, D_1 also starts to conduct at t_3 . Substituting (4.3) to (2.10), we get

$$(4.5) \quad q_1(t_3) = V_s \left[C_p + C_0 \left(1 + \frac{x_3}{x_0}\right) \right].$$

Stage IV:

From t_3 to t_4 , D_1 is conducting and ΔQ is transferred into C_1 from C_2 . At t_4 , $x(t_4) = -X_s = x(t_0)$ and the state of the doubler circuit is the same as when $t = t_0$, leading to

$$(4.6) \quad q_1(t_4) = q_1(t_0)$$

where

$$(4.7) \quad q_1(t_4) = q_1(t_3) + \Delta Q = V_s \left[C_p + C_0 \left(1 + \frac{X_s + 2x_3}{x_0}\right) \right].$$

From the equations (2.2), (4.6) and (4.7), the displacement at t_3 is given by $x_3 = 0$. As the consequence

$$(4.8) \quad \Delta Q = V_s C_0 \frac{X_s}{x_0}.$$

Substituting this result back into (2.10) and (2.11), the voltages across C_1 and C_2 at t_2 are obtained

$$(4.9) \quad V_1(t_2) = \frac{q_1(t_2)}{C_1(t_2)} = \frac{V_s(C_p + C_0)}{C_p + C_0(1 - \frac{X_s}{x_0})},$$

$$(4.10) \quad V_2(t_2) = \frac{q_2(t_2)}{C_2(t_2)} = \frac{V_s(C_p + C_0)}{C_p + C_0(1 + \frac{X_s}{x_0})}.$$

At t_2 , D_3 starts to stop conducting since V_1 is slightly less than $V_2 + V_s$. This relation can be approximated as $V_1 \approx V_2 + V_s$. Similarly as equation (4.1), we get

$$(4.11) \quad \frac{1 + \frac{C_0}{C_p}}{1 + \frac{C_0}{C_p} \left(1 - \frac{X_s}{x_0}\right)} = 1 + \frac{1 + \frac{C_0}{C_p}}{1 + \frac{C_0}{C_p} \left(1 + \frac{X_s}{x_0}\right)}.$$

The solution of the maximum displacement at steady state is

$$(4.12) \quad X_s = \frac{3(\sqrt{2} - 1)}{2} x_0.$$

Substituting (4.12) back into (4.1), the proof mass displacement at t_1 is determined by

$$(4.13) \quad x_1 = \frac{3}{2} \left(\sqrt{4 - 2\sqrt{2}} - 1 \right) x_0.$$

Therefore, the peak values of V_1 and V_2 are

$$(4.14) \quad V_I = V_1(t_2) = V_s \left(1 + \frac{1}{\sqrt{2}} \right),$$

$$(4.15) \quad V_{II} = V_2(t_1) = V_s \sqrt{1 - \frac{1}{\sqrt{2}}}.$$

V_1 and V_2 are then approximated by

$$(4.16) \quad V_1 = \frac{V_I + V_s}{2} + \frac{V_I - V_s}{2} \sin(\omega t) = V_s \left(1 + \frac{1}{2\sqrt{2}} \right) + V_s \frac{1}{2\sqrt{2}} \sin(\omega t),$$

$$(4.17) \quad V_2 = \frac{V_{II} + V_s}{2} - \frac{V_s - V_{II}}{2} \sin(\omega t) = V_s \frac{1 + \sqrt{1 - \frac{1}{\sqrt{2}}}}{2} - V_s \frac{1 - \sqrt{1 - \frac{1}{\sqrt{2}}}}{2} \sin(\omega t)$$

yielding

$$(4.18) \quad V_1^2 - V_2^2 = V_s^2 (\alpha + \gamma) [(\alpha - \gamma) + (\beta + \lambda) \sin(\omega t)] \left(1 + \frac{\beta - \lambda}{\alpha + \gamma} \sin(\omega t) \right)$$

where

$$(4.19) \quad \alpha = 1 + \frac{1}{2\sqrt{2}}, \beta = \frac{1}{2\sqrt{2}}, \gamma = \frac{1 + \sqrt{1 - \frac{1}{\sqrt{2}}}}{2}, \lambda = \frac{1 - \sqrt{1 - \frac{1}{\sqrt{2}}}}{2}.$$

Since $\frac{\beta - \lambda}{\alpha + \gamma} \approx 0.058 \ll 1$ is negligible and $\alpha - \gamma = \beta + \lambda$, the electrostatic force can be given by

$$(4.20) \quad F_e = \frac{1}{2} \frac{C_0}{x_0} V_s^2 (\alpha^2 - \gamma^2) (1 + \sin(\omega t)) = \frac{1}{2} \frac{C_0}{x_0} V_s^2 \frac{5(1 + \sqrt{2}) - 2\sqrt{4 - 2\sqrt{2}}}{8} (1 + \sin(\omega t))$$

which is represented as

$$(4.21) \quad F_e = F_0 (1 + \sin(\omega t))$$

where $F_0 = \frac{5(1 + \sqrt{2}) - 2\sqrt{4 - 2\sqrt{2}}}{16} \frac{C_0}{x_0} V_s^2$.

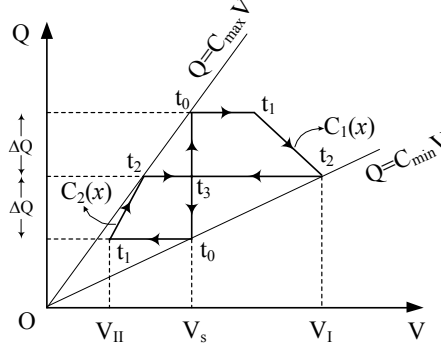


FIGURE 9. Q-V diagram of Bennet's doubler at steady-state for both variable capacitors.

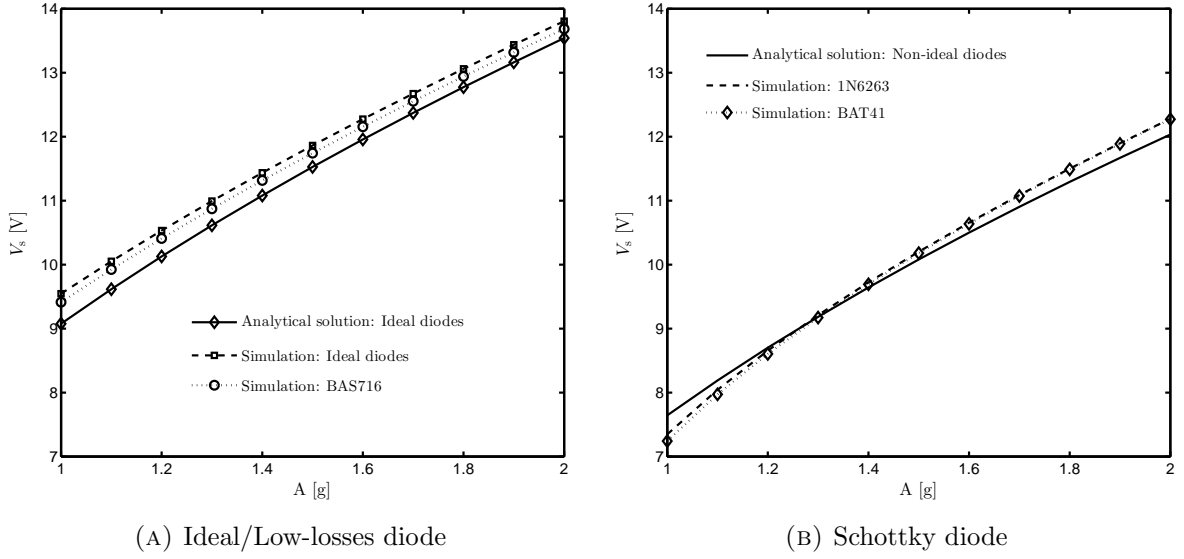


FIGURE 10. Acceleration responses of output voltages at steady state: a comparison between simulations and analytical solutions.

Using the same analysis procedure in the previous section, the saturation voltage is

$$(4.22) \quad V_s = \sqrt{\frac{16}{5(1+\sqrt{2})-2\sqrt{4-2\sqrt{2}}} \frac{mA - \frac{3}{2}(\sqrt{2}-1)x_0b\omega_0}{\frac{C_0}{x_0}}} \approx \sqrt{1.61 \frac{mA - \frac{3}{2}(\sqrt{2}-1)x_0b\omega_0}{\frac{C_0}{x_0}}}.$$

Based on those analysis above, the completed Q-V diagram combined by both transducers is summarized in Figure 9.

 TABLE 2. Diodes parameters: reverse saturation current I_s , zero-bias junction capacitance C_j and built-in junction voltage V_j

Diode	I_s [nA]	C_j [pF]	V_j [V]
1N6263	3.87	1.77	0.39
BAS716	3.52e-6	1.82	0.65
BAT41	10.00	5.76	0.37

4.2. **Numerical validations.** Figure 10a shows the saturation voltages for different acceleration amplitudes, where the simulation results with use of the mathematically idealized diode and the

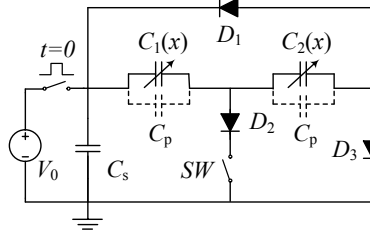


FIGURE 11. A new topology with single switch connected in series with the diode D_2 .

analytical solution expressed by formula (3.8) are compared. The figure also exhibits that the low-losses diode BAS716 performs very close to that of mathematically idealized diode. In the same manner, Figure 10b presents the comparison of the analytical solution obtained from (4.22) against the numerical simulations using different Schottky diodes. Despite of disparities in reverse current, junction capacitance and built-in junction voltage, both diodes 1N6263 and BAT41 give almost the same saturation voltages. The agreement between theoretical and numerical results in both cases verifies the predictions of our analytical approach and solutions. Diode parameters used on the simulations are listed in Table 2.

4.3. Effect of diode operation on mechanical dynamics. The Q-V cycle is a useful geometrical tool that enables us to realize the operation of voltage doubler circuit at steady state. However, the harvesting system performance in reality is more sophisticated, especially in transient time.

Based on dynamic simulations, we observe that the phases of the external force $F(t)$, the proof mass displacement $x(t)$ and the electrostatic force $F_e(t)$ are initially different. However, those differences gradually decrease due to effect of the diode states (i.e. blocked and conducting). This variation process leads to the negligible phase shift at steady state. Such a clarification supports the assumption that we made in theoretical analysis sections. In other words, the dynamic motion of the proof mass also strongly depends on both of the transducing force and the diode operation mechanism. This statement is valid when different diode models such as the mathematically idealized diode and the Schottky diodes are utilized.

5. CIRCUIT TOPOLOGIES TO IMPROVE THE SATURATION VOLTAGE

5.1. A new voltage doubler with single switch. Although the diode D_2 plays an vital role for initially charging C_1 , in principle, it could be removed after a few transient vibration cycles. This also enlarges the charging current through the storage capacitor due to the relation $I_{C_s} = I_{D_3} - I_{D_2}$. Therefore, it is worthwhile to investigate performance of the harvester when D_2 is disconnected. An electronic switch SW in series with D_2 can be used for this function, as shown in Figure 11.

In the simulation, SW is only *ON* in the first several vibration cycles, then turned *OFF* to eliminate effect of D_2 on I_{C_s} . Figure 12a shows evolution of the output voltage in two cases without and with presence of SW . Saturation voltage in the latter case is about ~ 15.60 V. This is a significant improvement over the 13.84 V achieved for the circuit topology in Figure 2. Similar results are obtained with different acceleration amplitudes in Figure 12b.

5.2. Cockcroft-Walton generator applied to MEMS device. A common topology of voltage doubler further developed from the Greinacher circuit [28] is depicted in Figure 13, in which the feedback diode D_2 is added to connect the storage capacitor and the two transducers. Both theoretical operation analysis and simulation results show that performances of the Bennet's doubler and the

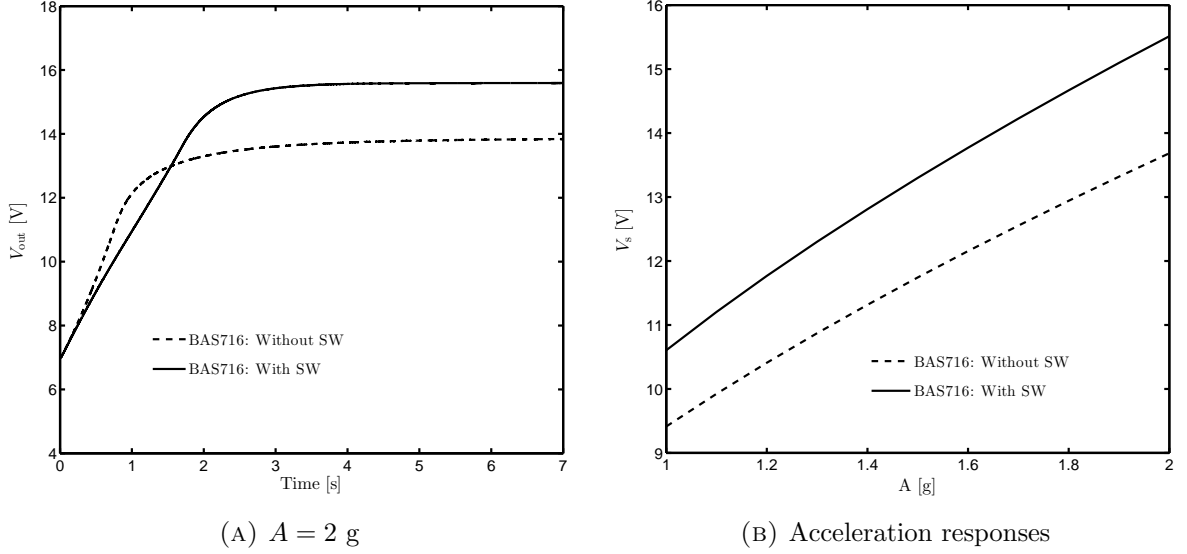


FIGURE 12. (a) The time evolution of output voltage at $A = 2$ g and (b) The saturation voltage versus acceleration amplitudes, comparison of two cases: with and without the switch.

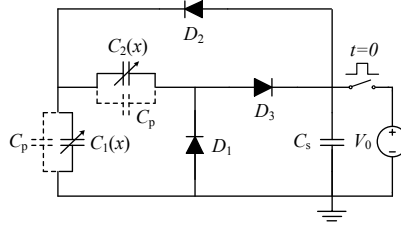


FIGURE 13. An adapted configuration of the Greinacher's doubler.

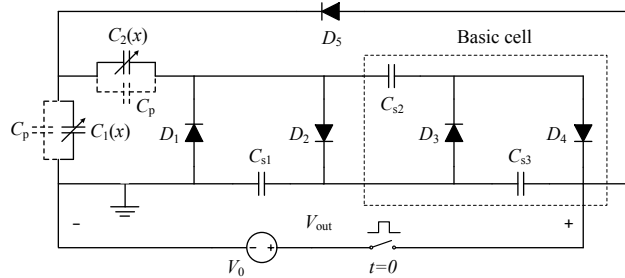


FIGURE 14. The two-stage Cockcroft-Walton multiplier.

Greinacher configuration are completely identical. The roles of three diode D_1 , D_2 and D_3 are the same as they do in Figure 2.

Based on the Greinacher doubler circuit, a well-known voltage cascade was early proposed by the British and Irish physicists John D. Cockcroft and Ernest T. S. Walton in 1932 [29, 30]. The Cockcroft-Walton generator (i.e., named after the two authors) was proved to be able to generate a high DC voltage from a low-voltage AC, which therefore is interesting to be utilized for the micro-scale harvesters. Figure 14 shows the circuit diagram of the two-stage Cockcroft-Walton, in which the voltage across two capacitor C_{s1} and C_{s3} is the output voltage, called V_{out} . The simplified operation of such a multi-stage voltage doubler is depicted in Figure 15. Similar to the Bennet's

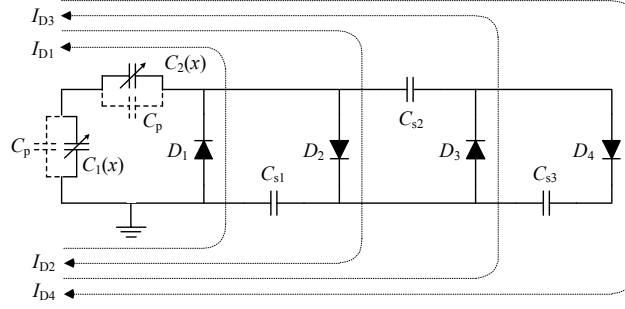


FIGURE 15. Main operation of the two-stage Cockcroft-Walton multiplier.

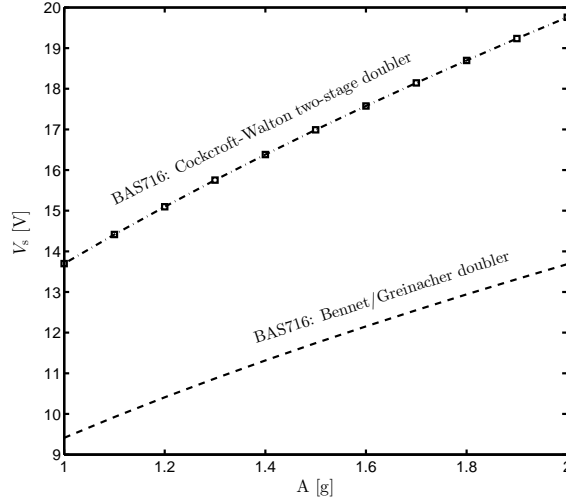


FIGURE 16. Comparison of the saturation voltage versus acceleration amplitude for the Bennet's doubler and the two-stage Cockcroft-Walton voltage multiplier.

configuration, operation of the Cockcroft-Walton multiplier can also be divided into a sequence of four stages. At first, all diodes are blocked. In the second stage, D_1 and D_3 are simultaneously conducting and charges are transferred to C_2 and C_{s2} . All diodes are reverse-biased in the third stage. In the final stage, D_2 and D_4 are conducting, transferring the scavenged energy to C_{s1} and C_{s3} . D_5 is mainly used for pre-charging C_1 and its conduction during operation is insignificant and negligible.

Figure 16 shows a remarkable increase of the saturation voltage when the Cockcroft-Walton multiplier and the Bennet's doubler are compared. Since the topology discussed in Section 5.1 requires a control unit for controlling the switch, the Cockcroft-Walton multiplier is much more convenient to keep the simplicity in practical implementation. Furthermore, our simulations reveal that this circuit topology is capable of operating with a very low ratio of capacitance variation $\eta < 2$. In particular, its minimum value is found $\eta_{\min} = 1.52$, making such a circuit attractive for further investigation in future work.

6. CONCLUSION

This study presented a theoretical analysis of MEMS electrostatic energy harvesters configured as Bennet's doubler at saturation regime, based on combination of Q-V diagram and dynamic simulations. The steady state operation of voltage doubler was approximately determined as a

right-angled trapezoidal conversion cycle. Mathematically idealized and non-ideal diode models were investigated, resulting in different analytical solutions of the saturation voltages. The theoretical approach was verified by circuit simulation results obtained from a complete model of the harvesting system. An essential effect of the diode operation mechanism to the in-phase behavior of the input mechanical vibration and the electrostatic force was discussed. A similarity of Bennet's doubler and resistive fly-back charge-pump circuit is realized by comparing their Q-V diagram. An alternative circuit using a single switch was introduced, where the saturation voltage was significantly improved in comparison with the conventional topologies. The Cockcroft-Walton multiplier is another promising solution since it shows a potential to work with MEMS harvesters that have small varying capacitance ratio.

REFERENCES

- [1] C. Sergiou, P. Antoniou, and V. Vassiliou, "A comprehensive survey of congestion control protocols in wireless sensor networks," *IEEE Communications Surveys Tutorials*, vol. 16, pp. 1839–1859, Fourthquarter 2014.
- [2] I. Khan, F. Belqasmi, R. Glitho, N. Crespi, M. Morrow, and P. Polakos, "Wireless sensor network virtualization: A survey," *IEEE Communications Surveys Tutorials*, vol. 18, pp. 553–576, Firstquarter 2016.
- [3] N. E. duToit, B. L. Wardle, and S. G. Kim, "Design considerations for MEMS-scale piezoelectric mechanical vibration energy harvesters," *Integrated Ferroelectrics*, vol. 71, pp. 121–160, July 2005.
- [4] Beeby, Torah, Tudor, Glynne-Jones, O'Donnell, Saha, and Roy, "A micro electromagnetic generator for vibration energy harvesting," *Journal of Micromechanics and Microengineering*, vol. 17, no. 7, pp. 1257–1265, 2007.
- [5] Y. Chiu, C.-T. Kuo, and Y.-S. Chu, "MEMS design and fabrication of an electrostatic vibration-to-electricity energy converter," *Microsystem Technologies*, vol. 13, no. 11, pp. 1663–1669, 2007.
- [6] S. Roundy, P. K. Wright, and J. Rabaey, "A study of low level vibrations as a power source for wireless sensor nodes," *Computer Communications*, vol. 26, pp. 1131–1144, July 2003.
- [7] V. P. Dragunov and D. I. Ostertak, "Microelectromechanical converters," *Russian Microelectronics*, vol. 41, no. 2, pp. 107–121, 2012.
- [8] B. C. Yen and J. H. Lang, "A variable-capacitance vibration-to-electric energy harvester," *IEEE Transactions on Circuits and Systems—Part I: Regular Papers*, vol. 53, pp. 288–295, Feb. 2006.
- [9] P. D. Mitcheson, T. C. Green, and E. M. Yeatman, "Power processing circuits for electromagnetic, electrostatic and piezoelectric inertial energy scavengers," *Microsystem Technologies*, vol. 13, no. 11, pp. 1629–1635, 2007.
- [10] A. Bennet and R. Kaye, "An account of a doubler of electricity, or a machine by which the least conceivable quantity of positive or negative electricity may be continually doubled, till it becomes perceptible by common electrometers, or visible in sparks. by the Rev. Abraham Bennet, M. A.; communicated by the Rev. Richard Kaye, LL. D. F. R. S.," *Philosophical Transactions of the Royal Society of London*, vol. 77, pp. 288–296, 1787.
- [11] A. C. M. de Queiroz and M. Domingues, "Electrostatic energy harvesting using doublers of electricity," in *Circuits and Systems (MWSCAS), 2011 IEEE 54th International Midwest Symposium on*, pp. 1–4, Aug 2011.
- [12] A. C. M. de Queiroz and M. Domingues, "The doubler of electricity used as battery charger," *IEEE Transactions on Circuits and Systems II: Express Briefs*, vol. 58, pp. 797–801, Dec 2011.
- [13] A. C. M. de Queiroz and M. Domingues, "Analysis of the doubler of electricity considering a resistive load," in *Circuits and Systems (MWSCAS), 2013 IEEE 56th International Midwest Symposium on*, pp. 45–48, Aug 2013.
- [14] V. Dragunov and V. Dorzhiev, "Electrostatic vibration energy harvester with increased charging current," *Journal of Physics: Conference Series*, vol. 476, no. 1, p. 012115, 2013.
- [15] E. Lefeuvre, S. Riskey, J. Wei, M. Woytasik, and F. Parrain, "Self-biased inductor-less interface circuit for electret-free electrostatic energy harvesters," *Journal of Physics: Conference Series*, vol. 557, no. 1, p. 012052, 2014.
- [16] V. Dorzhiev, A. Karami, P. Basset, F. Marty, V. Dragunov, and D. Galayko, "Electret-free micromachined silicon electrostatic vibration energy harvester with the bennet 's doubler as conditioning circuit," *IEEE Electron Device Letters*, vol. 36, pp. 183–185, Feb 2015.

- [17] E. Lefeuvre, J. Wei, H. Mathias, and F. Costa, "Single-switch inductorless power management circuit for electrostatic vibration energy harvesters," in *New Circuits and Systems Conference (NEWCAS), 2015 IEEE 13th International*, pp. 1–4, June 2015.
- [18] D. Galayko, *Conditioning Circuits for Capacitive Energy Harvesters*, pp. 239–277. Cham: Springer International Publishing, 2016.
- [19] C. P. Le and E. Halvorsen, "Mems electrostatic energy harvesters with end-stop effects," *Journal of Micromechanics and Microengineering*, vol. 22, no. 7, p. 074013, 2012.
- [20] B. D. Truong, C. P. Le, and E. Halvorsen, "Analysis of electrostatic energy harvesters electrically configured as Bennet's doublers," *IEEE Sensors Journal*, vol. 17, pp. 5180–5191, Aug 2017.
- [21] S. G. Burrow, P. D. Mitcheson, and B. H. Stark, *Power Conditioning Techniques for Energy Harvesting*, pp. 323–343. New York, NY: Springer New York, 2013.
- [22] S. G. Burrow and P. D. Mitcheson, *Power Conditioning for Energy Harvesting - Theory and Architecture*, pp. 85–101. Wiley-VCH Verlag GmbH & Co. KGaA, 2015.
- [23] S. Roundy, K. S. J. Pister, and P. K. Wright, "Micro-electrostatic vibration-to-electricity converters," in *Proceedings of IMECE2002*, ASME International Mechanical Engineering Congress & Exposition, ASME, November 2002.
- [24] H. R. Florentino, D. Galayko, R. C. S. Freire, B. A. Luciano, and C. Florentino, "Energy Harvesting Circuit Using Variable Capacitor with Higher Performance," *Journal of Integrated Circuits and Systems*, vol. 6, no. 1, pp. 68–74, 2011.
- [25] E. O'Riordan, A. Dudka, D. Galayko, P. Basset, O. Feely, and E. Blokhina, "Capacitive energy conversion with circuits implementing a rectangular charge-voltage cycle part 2: Electromechanical and nonlinear analysis," *IEEE Transactions on Circuits and Systems I: Regular Papers*, vol. 62, pp. 2664–2673, Nov 2015.
- [26] M. H. Bao, *Micro Mechanical Transducers Pressure Sensors, Accelerometers and Gyroscopes*, vol. 8 of *Handbook of Sensors and Actuators*. Elsevier, 2000.
- [27] D. V. Pavlovich and D. V. Yuryevich, "Influence of diodes parameters on the operation of e-veh circuit based on bennet's doubler," *PROCEEDINGS OF THE RUSSIAN HIGHER SCHOOL ACADEMY OF SCIENCES*, vol. 31, no. 2, 2015.
- [28] W. Hauschild and E. Lemke, *High-Voltage Test and Measuring Techniques*. Springer-Verlag Berlin Heidelberg, 1 ed., 2014.
- [29] J. D. Cockcroft and E. T. S. Walton, "Experiments with high velocity positive ions. (i) further developments in the method of obtaining high velocity positive ions," *Proceedings of the Royal Society of London A: Mathematical, Physical and Engineering Sciences*, vol. 136, no. 830, pp. 619–630, 1932.
- [30] J. D. Cockcroft and E. T. S. Walton, "Experiments with high velocity positive ions. ii. the disintegration of elements by high velocity protons," *Proceedings of the Royal Society of London A: Mathematical, Physical and Engineering Sciences*, vol. 137, no. 831, pp. 229–242, 1932.